Structure changes in ^{160}Er from low to ultrahigh spin

J. Ollier, J. Simpson, M.A. Riley, E.S. Paul, X. Wang, A. Aguilar, M.P. Carpenter, I.G. Darby, D.J. Hartley, R.V. F. Janssens, F.G. Kondev, T. Lauritsen, P.J. Nolan, M. Petri, J.M. Rees, S.V. Rigby, C. Teal, J. Thomson, C. Unsworth, S. Zhu, A. Kardan, and I. Ragnarsson

Phys. Rev. C **83**, 044309 — Published 12 April 2011

DOI: 10.1103/PhysRevC.83.044309

The changing structure of ^{160}Er from low to ultrahigh spin

J. Ollier,[1] J. Simpson,[1] M. A. Riley,[2] E. S. Paul,[3] X. Wang,[2] A. Aguilar,[2] M. P. Carpenter,[4] I. G. Darby,[5,*] D. J. Hartley,[6] R. V. F. Janssens,[4] F. G. Kondev,[4] T. Lauritsen,[4] P. J. Nolan,[3] M. Petri,[3,†] J. M. Rees,[3] S. V. Rigby,[3] C. Teal,[2] J. Thomson,[3] C. Unsworth,[3] S. Zhu,[4] A. Kardan,[7,8] and I. Ragnarsson[8]

[1]*STFC Daresbury Laboratory, Daresbury, Warrington, WA4 4AD, UK*
[2]*Department of Physics, Florida State University, Tallahassee, Florida 32306, USA*
[3]*Oliver Lodge Laboratory, University of Liverpool, Liverpool L69 7ZE, UK*
[4]*Nuclear Engineering Division and Physics Division, Argonne National Laboratory, Argonne, Illinois 60439, USA*
[5]*Department of Physics and Astronomy, University of Tennessee, Knoxville, Tennessee 37996*
[6]*Department of Physics, U. S. Naval Academy, Annapolis, Maryland 21402, USA*
[7]*Physics Department, Faculty of Science, Ferdowsi University of Mashhad, P.O. Box 91775-1436, Mashhad, Iran*
[8]*Division of Mathematical Physics, LTH, Lund University, Post Office Box 118, S-22100 Lund, Sweden*

A spectroscopic investigation of the γ decays from excited states in ^{160}Er has been performed in order to study the changing structural properties exhibited from low spin up towards ultrahigh spin ($I \sim 60\hbar$). The nucleus ^{160}Er was populated by the reaction ^{116}Cd(^{48}Ca,4nγ) at a beam energy of 215 MeV and resulting γ decays were studied using the Gammasphere spectrometer. New rotational structures and extensions to existing bands were observed, revealing a diverse range of quasiparticle configurations, which are discussed in terms of the cranked shell model. At spins around $50\hbar$ there is evidence for oblate states close to the yrast line. Three rotational bands that have the characteristics of strongly deformed triaxial structures are observed, marking a return to collectivity at even higher spin. The high spin data are interpreted within the framework of cranked Nilsson-Strutinsky calculations.

PACS numbers: 27.70.+q,21.10.Re,23.20.Lv

I. INTRODUCTION

Advances in γ-ray spectroscopy have opened the possibility of performing discrete-line spectroscopy from the nuclear ground state up to ultrahigh spin ($I \sim 60\hbar$). Spectroscopic studies over such a large spin range reveal a diverse spectrum of nuclear structure phenomena. The transitional rare-earth nuclei near $N = 90$ and A ≈ 160 are particularly rich in such phenomena. In this region, the yrast structure, at low spins, is formed from a series of rotational bands based on a deformed collective prolate shape. As these structures are rotated a complex picture of band crossings emerges, the first discovered in ^{160}Dy by Johnson *et al.* [1] and later interpreted as an alignment of a pair of high-j $i_{13/2}$ neutrons [2]. Determining the nature of such alignments can help identify the underlying configurations of the single-particle orbitals involved. This region of the nuclear chart is dominated by rotational bands and band crossings below spin $\approx 40\hbar$, which are understood in terms of their underlying quasiparticle structures within the framework of the cranking model based on the Woods-Saxon potential [3, 4].

At higher spin, the yrast structure of these nuclei can undergo a dramatic change with the transition from a prolate to an oblate shape [5–13]. Here non-collective single-particle configurations become energetically favored via the mechanism of band termination [14, 15].

Recently, further structural changes have been observed at even higher spin with the discovery of rotational band sequences that appear to bypass the band-terminating states and push discrete-line spectroscopy into the ultrahigh spin domain [16]. Comparison with results from cranked Nilsson-Strutinsky (CNS) calculations suggest that these collective structures are based on configurations that arise from triaxial strongly deformed (TSD) shapes. There are now several examples of these rotational structures in this mass region [17–20].

The present experimental work was performed in order to carry out a detailed spectroscopic investigation of $^{160}_{68}$Er$_{92}$. Previous work has exposed a wide variety of rotational and vibrational bands [21–23] in this nucleus and its yrast structure has been observed up to $\sim 50\hbar$ [24, 25]. The present article reports on the observation of new rotational bands and extensions to existing structures and discusses these in the framework of the cranked shell model. Extensions

*Present address: Instituut voor Kern-en Stralingsfysica, Katholieke Universiteit Leuven, B-3001 Leuven, Belgium
†Present address: Nuclear Science Division, Lawrence Berkeley National Laboratory, Berkeley, California 94720, USA

to the lowest-energy positive- and negative-parity bands are discussed in terms of the transition towards oblate structures at high spin. The present experiment has revealed three new rotational bands, predicted to be based on strongly deformed triaxial configurations, two of which have been published previously [20], and these extend the yrast structure towards ultrahigh spin.

II. EXPERIMENTAL DETAILS

The experiment was performed using the ATLAS facility at Argonne National Laboratory. Excited states in ^{160}Er were populated using a 215-MeV beam of ^{48}Ca incident upon enriched (98.7%) targets of ^{116}Cd, inducing fusion-evaporation reactions. The target comprised of two self-supporting ^{116}Cd foils with a total thickness of 1.3 mg/cm^2. The γ decays resulting from the reaction products were detected using the Gammasphere γ-ray spectrometer [26, 27]. A total of $\sim 1.9\times10^9$ events were collected when at least seven of the 101 Compton-suppressed HPGe detectors fired in prompt coincidence. The data were collected over a five day period. Unfolding the events resulted in approximately 1.4×10^{11} triple and 3.5×10^{10} quadruple coincidence events, which were replayed off-line into RadWare-format three-dimensional (E^3_γ) cubes [28] and four-dimensional (E^4_γ) hypercubes [29] for analysis.

One-dimensional spectra were also unfolded directly from the data using the technique discussed in Ref. [30]. They were produced with multiple gates set on inband stretched quadrupole (E2) transitions from ^{160}Er up to fold seven (γ^7) where the data was further separated into the corresponding detectors in the rings of Gammasphere at a fixed angle θ to the beam direction. Angle-specific spectra were then analysed to obtain angular intensity ratios and, based on the directional correlations from oriented states method [31], were used to distinguish between stretched quadrupole and dipole γ-ray transitions. The ratio R of the intensity of transitions at $\sim 130°(50°)$ and 90° to the beam direction was measured and is given by

$$R = \frac{I_\gamma[\theta \sim 130°(50°)]}{I_\gamma[\theta \sim 90°]}. \quad (1)$$

This ratio is approximately a factor of two larger for stretched quadrupole than for stretched dipole transitions.

III. RESULTS

The ^{160}Er level scheme constructed from the present work is given in Fig. 1 and a summary of the measurements obtained is presented in Table I. The energies of the candidate TSD bands can be found in Table II.

A. Positive-parity bands: Yrast band, bands 3, 4 and 5

The lowest-energy band, based on the ground state, has (parity, signature) $(\pi, \alpha) = (+, 0)_1$ and is yrast at low spin (also labeled yrast in Fig. 1), has previously been reported to $I^\pi = 50^+$ [24]. This was further extended to (54^+) by Kondev *et al.* [25] although no explicit transition energies were published. The present work is in agreement with these previous works up to (48^+). A γ-ray spectrum showing the high-energy part of the yrast band is presented in Fig. 2(a). The photopeaks corresponding to the γ decays of the excited states from 36^+ (1011 keV) to (48^+) (1284 keV) are well defined in this spectrum. In addition, seven weakly populated photopeaks are observed at higher energies that are in coincidence with the yrast band and lie at higher spin. Due to the lack of statistics, it was not possible to determine distinct coincidences between these photopeaks nor to order them, however the 1345 keV transition tentatively extends the band up to (50^+) based on the intensity profiles shown in Fig. 3(a). It was not possible to confirm the extension of the band to (54^+), as proposed in [25].

Excited states up to $34\hbar$ in the $(+, 0)_2$ band, band 3, were reported previously [24]. Seven new transitions were observed in the present work extending this band up to a possible (46^+) level. The spectrum in Fig. 4(a) was produced from a sum of triple gates set in the E^4_γ hypercube and shows all of the transitions observed in the band. It also indicates that the band is in coincidence with the yrast band up to the 16^+ state. Fig. 4(b) was produced by a double gate set on the 1045 and 1079 keV transitions, and demonstrates the presence of the 1079/1082 keV doublet shown in the level scheme of Fig. 1. The 859 keV transition observed by Simpson *et al.*,[21] as the decay of the $30^+ \rightarrow 28^+$ excited state in this band was not observed in coincidence with transitions above the 24^+ state. In the present work, it has not been assigned to this band, but as a 860 keV linking transition to band 4, see Fig. 1. The multipolarity of the 723 keV linking transition was measured and found to be of a stretched quadrupole character (see Table I), confirming the previous measurement [21] and the assignment of positive parity to band 3.

A new positive parity band, labeled band 4 in Fig. 1, which decays into the yrast band and band 3, was observed. A γ-ray spectrum showing the transitions found in this new band is presented in Fig. 4(c). This spectrum provides evidence of photopeaks at 842 and 904 keV corresponding to transitions observed in band 3, indicating that band 3 and 4 are linked, with the 765 keV transition linking the (26^+) state in band 3 to the (24^+) state in band 4, and the 860 keV linking band 4 to band 3, as mentioned above. The spectrum of Fig. 4(c) also contains transitions in the yrast band up to the 14^+ state, which is populated by the 1033 keV linking transition. From the angular intensity ratio measurement (Table I) the multipolarity of this transition was found to be of a stretched quadrupole nature, confirming positive parity and even spin for this new band.

In addition, new transitions have been observed associated with the positive-parity odd-spin band, labeled band 5 in Fig. 1. Spectra showing transitions in this band are found in Fig. 5(a) and (b). A total of fifteen new in-band transitions and three new linking transitions were observed extending the band from the previously known (13^+) state [21, 22] up to a possible (43^+) state. The 907, 970 and 1020 keV γ rays connect this band to the yrast band and are labeled with triangles in Fig. 5(a).

B. Negative-parity bands 1, 2 and 6

Figures 2(b) and (c) present the high energy part of the negative-parity bands with $(-,0)_1$ and $(-,1)_1$ labeled band 1 and band 2 in Fig. 1, respectively. Good agreement was found between the γ rays observed in the present work and the previously published high-spin states [24] up to spin values of (48^-) in band 1 and (47^-) in band 2. Band 1 has also been reported up to a possible (54^-) by Kondev *et al.* [25], although no explicit transition energies were published. In the present work, the 1358 keV transition was observed as the candidate for the (50^-) state in band 1 (and a possible (52^-) state with the tentative 1465 keV transition) and the 1359 keV transition extends band 2 up to (49^-). Figures 2(b) and (c) indicate that there is a rapid decrease in intensity at the top of the bands with possible weak candidates for transitions feeding the bands from higher spin, indicated in parentheses in the spectra. This drop in intensity is also demonstrated in Fig. 3(b), where the relative intensities of these transitions are plotted.

A previous experimental study by Sweeney *et al.*, [32] observed a band associated with the γ decay of ^{160}Er, that was not connected to the known level scheme. In the present study, this band, labeled band 6 in Fig. 1, has been linked to the yrast band and extended to higher spin by five new transitions. Fig. 5(c) gives a γ-ray spectrum produced with a sum of triple gates set on transitions observed in band 6. The three linking transitions observed at 1140, 1033 and 910 keV, labeled with triangles in Fig. 5(c), establish the band head energy at 1905 keV. The angular intensity ratio extracted for the 387 keV transition that links the 8^- state of band 1 to band 6 and was found to be of a stretched quadrupole nature, see Table I. Although a large error was associated with this measurement, it suggests that band 6 has negative-parity and even-spin levels beginning at 6^- and extending up to (36^-).

C. The strongly coupled bands

Bands 7 and 8 in Fig. 1 were previously observed and reported in Ref. [23], but were not linked to the main level scheme. In the present work, two tentative linking transitions have been observed at 901 and 764 keV, the former can be seen in Fig. 6(a). Therefore, bandhead energies of 3240 keV and 3461 keV have been tentatively deduced for bands 7 and 8, respectively. The multipolarity of these linking transitions could not be established through angular intensity measurements due to low statistics, however, bands 7 and 8 have tentatively been assigned positive parity, see discussion below. The level energies for these bands indicate spin assignments at $\sim 13-14\hbar$. For larger initial spin values, the bands would become yrast at higher spin, which is contrary to the intensity measurements in Table I. Therefore, an I^π of 13^+ and 14^+ is tentatively assigned to the bandheads of bands 7 and 8, respectively.

Two other strongly coupled bands were also reported in [23]. One of these was connected to the yrast band at low spin and the other was a higher spin "floating" structure. In the discussion, these bands were interpreted as being connected, but the gap of $\sim 8\hbar$ was not established. In the present work these previous sequences have been connected forming bands 9 and 10, see Fig. 1. A γ-ray spectrum, with most of the transitions within the bands, is presented in Fig. 6(b). An angular intensity ratio was extracted for the 1386 keV transition that links band 9 to the 6^+ yrast state, and was found to be of a stretched dipole nature, albeit with a large error, see Table I. Further angular intensity measurements were extracted for the 175, 204, 226 and 235 keV transitions, which link bands 9 and 10 at low spins. These measurements confirm the dipole nature of the inter-band transitions and negative parity has been assigned to these strongly coupled structures.

Two new bands are also reported in this work, bands 11 and 12 in Fig. 1. Fig. 6(c) is a γ-ray spectrum produced by a triple gate set on transitions within band 11. Transitions associated with bands 9 and 10 can also be seen in this spectrum, confirming that they are linked. Transitions from band 12 can be observed in the γ-ray spectrum of

Fig. 6(b). The transitions at the top of band 11 and most of the transitions associated with band 12 have very low intensities and are marked as tentative. Angular intensity ratios were not extracted from the present data for the linking transitions for these bands due to low statistics. However, a tentative assignment of positive parity has been made for these bands, see the following discussion.

D. TSD 3

Two bands associated with the γ decay of ^{160}Er and with high moments-of-inertia were observed in the present experimental work and reported previously in Ref. [20]. These are labeled TSD 1 and TSD 2 in Fig. 1. These bands are possible candidates for configurations based on triaxial strongly deformed structures that compete for yrast status at the highest spin [16]. Further analysis of the data has revealed a new band with similar high moment-of-inertia characteristics as the previous two. This band is labeled TSD 3 in Fig. 1 and a γ-ray spectrum produced with a sum of triple gates is given in Fig. 7.

This band consists of nine transitions and three tentative ones at higher energy. The photopeak at 1257 keV in Fig. 7 is a possible candidate for the decay of this band to the main level scheme. The yrast transitions up to the decay of the 20^+ state are observed in this spectrum, confirming its association with ^{160}Er and suggesting a bandhead spin of > 20.

IV. DISCUSSION

The nucleus $^{160}_{68}\mathrm{Er}_{92}$ is fourteen nucleons outside of the doubly-magic $^{146}_{64}\mathrm{Gd}_{82}$ core and its low spin structure is dominated by collective rotation of a prolate deformed shape. Indeed, its $E(4_1^+)/E(2_1^+)$ ratio of ~ 3.1 is close to that of a perfect rotor (3.33). In addition, the Fermi level for $N = 92$ lies near the bottom of the $N_{\mathrm{osc}} = 6(\nu i_{13/2})$ shell and it is the occupation of these low-Ω $i_{13/2}$ orbitals that helps drive the prolate deformation in this region. The present work provides the level scheme of Fig. 1 with a diverse range of rotational bands, some of which extend to high spin.

To help understand the characteristics of each band and identify the underlying configurations, Woods-Saxon cranked shell-model (CSM) calculations [3, 4] have been performed for ^{160}Er. The resulting quasiparticle trajectories for the neutrons and protons are presented in Fig. 8(a) and (b), respectively. Table III gives the labeling scheme for the orbitals involved in the following discussion.

The aligned angular momentum (or alignment) [33] as a function of rotational frequency and the excitation energy relative to that of a rotating liquid drop (based on the Lublin Strasbourg model [34, 35]) as a function of spin, are plotted for the bands in ^{160}Er in Figs. 9, 10, 11 and 12. In the aligned angular momentum plots a "natural reference" [36] was subtracted. This is based on Harris parameters [37, 38] extracted from variable moment of inertia (VMI) fits to the ground-state structure, with values of $J_0 = 23\hbar^2\mathrm{MeV}^{-1}$ and $J_1 = 58\hbar^4\mathrm{MeV}^{-3}$.

The most probable quasiparticle configurations, based on the following discussion for all of the bands, are summarized in Table IV.

A. Positive-parity bands: Yrast band, bands 3, 4 and 5

The behavior of the yrast band has previously been discussed in terms of the ground-state configuration (vacuum state) undergoing the first $(i_{13/2})^2$ neutron alignment, the AB crossing, at a rotational frequency $\hbar\omega \sim 0.28$ MeV, followed by the first $(h_{11/2})^2$ proton alignment, the A_pB_p crossing, at $\hbar\omega \sim 0.48$ MeV [21]. The yrast band is plotted in Figs. 9, 10, 11 and 12 where comparisons with other configurations can be made. It should be noted that the alignment gain of the A_pB_p crossing is greater, by $\sim 2\hbar$, than that observed in the negative parity bands 1 and 2 and in the neighboring nuclei [21, 40]. This may be an indication for an additional alignment. From the results of the CSM calculations for neutrons, Fig. 8(a), the EF $(f_{7/2}/h_{9/2})^2$ orbitals and/or the CD $(i_{13/2})^2$ orbitals, may also be active at these high rotational frequencies and be responsible for this additional gain in alignment.

The low-spin states of band 5 have previously been discussed in terms of being based on the odd spin γ-vibrational structure [22, 39]. The present work has pushed this band up to high spin (43^+) and Fig. 9(a) demonstrates that the alignment of band 5 follows the yrast band remarkably closely over a large frequency range. Band 5 experiences both the AB and the A_pB_p crossings. Both of these crossings occur at a slightly earlier frequency than in the yrast band, which may be explained as due to the higher excitation energy of band 5 compared with the yrast band, also apparent in Fig. 9(b). This is the first reported observation of a rotational band being built on the γ-vibrational structure going up to such high spins. It is worth noting that the even-spin γ-vibrational structure reported in Ref.

[22] was not observed in this work since it is at relatively high excitation energy compared with the yrast even-spin states and hence not populated in the present reaction.

The alignment and energy relative to a rotating liquid drop for bands 3 and 4 are provided in Fig. 10(a) and (b), respectively. Band 3 has previously been discussed in terms of the continuation of the ground-state band beyond the first neutron AB crossing, with the alignment gain attributed to a four quasineutron configuration $BCAD$ up to spin 24^+ [21]. The gain in alignment beyond the AB crossing is rather complex and further gains are established in the present work. The gain in alignment at $\hbar\omega \sim 0.53$ MeV is comparable with that expected for the $h_{11/2}$ A_pB_p crossing, but it occurrs at a delayed frequency, see Fig. 11 which shows this crossing clearly in the negative-parity bands 1 and 2. In addition, the $(f_{7/2}/h_{9/2})^2$ EF crossing may also be present in the overall alignment at these high rotational frequencies. It is noted that the EF crossing has been used to interpret similar alignment gains in the positive-parity yrare bands of the heavier $N = 94$ isotones ^{164}Yb [41] and ^{166}Hf [42].

The nature of the new band, band 4, which interacts with band 3 at $\hbar\omega \sim 0.4$ MeV, see Fig. 1, is uncertain. Above $\hbar\omega \sim 0.3$ MeV, band 4 has a larger alignment than band 3 and the AB configuration of the yrast band, see Fig. 10(a). This may indicate that band 4 is associated with at least, a two quasiparticle configuration coupled to a vibrational excitation; a structure of this nature has been observed in ^{128}Ce [43]. A possible explanation for this structure may lie with the β-vibrational band, also plotted in Figs. 10(a) and (b), which was established previously up to 3.369 MeV, $I^\pi = 14^+$ [22, 39]. In these plots band 4 appears to be a continuation of the β-vibrational band, with the gain in alignment caused by the AB crossing. However, this conjecture cannot be confirmed in the present work since neither the connection nor the β-band itself could be identified. In addition, band 4 was not observed to high enough a rotational frequency to identify the A_pB_p crossing.

B. Negative-parity bands 1, 2 and 6

The two lowest energy negative-parity bands, band 1 (-,0) and band 2 (-,1), have previously been discussed in terms of being based, at low rotational frequency, on the two quasineutron configurations AF and AE, respectively [21]. These two bands undergo the BC neutron alignment at $\hbar\omega \sim 0.3$ MeV and the A_pB_p proton alignment at $\hbar\omega \sim 0.45$ MeV, see Fig. 11.

Band 6 has an alignment at low frequency similar to bands 1 and 2, suggesting a two quasiparticle configuration. It also exhibits a gain in alignment at $\hbar\omega \sim 0.3$ MeV, which is consistent with the BC crossing, and a sharp alignment gain at $\hbar\omega \sim 0.41$ MeV, consistent with the A_pB_p crossing. The frequency where the A_pB_p crossing occurs is lower for band 6 than for bands 1 and 2, however, this can be explained by the higher excitation energy of band 6 compared with the other two, see Fig. 11(b), or it may be due to a lower deformation. Band 6 is, therefore, assigned as being based on the next lowest energy two quasineutron negative-parity configuration, AG.

C. Strongly coupled structures

The strongly-coupled signature-partner bands observed in ^{160}Er have previously been discussed in terms of being based on multi-quasiparticle excitations involving the $\pi h_{11/2}[523]7/2$ and $\pi g_{7/2}[404]7/2$ configurations [23]. The assignments made were strengthened through the ratios of the reduced transition probabilities B($M1$)/B($E2$), which can be deduced from measured (I$\rightarrow I-1$) to (I$\rightarrow I-2$) branching ratios. In the present work, the strongly coupled bands observed previously have been extended and placed in the level scheme and a new strongly coupled sequence has been added. The B($M1$)/B($E2$) values have also been measured and they are given for bands 7, 8, 9 and 10 in Fig. 13. Theoretical predictions for specific configurations are also presented in this figure using the semi-classical geometric model [44, 45]. The parameters used (g_R, i_x, and Q_0) were adopted from Ref. [23].

The strongly coupled sequence, band 7 and 8, was observed previously [23] (labeled band 3 in this previous work) and was interpreted at low rotational frequency as the $AE \otimes A_pE_p(F_p)$ configuration. The alignment plot of Fig. 12(a) shows that this band has a crossing at ~ 0.32 MeV, which is interpreted as the BC crossing. The proton crossing A_pB_p is not observed in bands 7 and 8, which is consistent with the presence of the A_p proton orbital in the quasi-particle configuration for these bands. The B($M1$)/B($E2$) ratios, Fig. 13, are not only consistent with the previous work [23], but are also characterized by an improved accuracy. The alignment plots and the B($M1$)/B($E2$) ratios agree well with each other and confirm the previous interpretation for this strongly coupled band [23], which is also consistent with the tentative spin assignments.

The low spin states of bands 9 and 10 were observed and reported in Ref. [23] (labeled band 1 in this previous work) and interpreted as associated with the two quasiproton configuration $A_pE_p(F_p)$. In the present work, these bands are extended up to ($34^-/35^-$) and undergo an alignment at $\hbar\omega \sim 0.28$ MeV, see Fig. 12(a), which is interpreted as the AB crossing. The present work delineates this alignment and connects the low spin part of this band to the

higher spin portion which was "floating" in the previous work [23], where the states were labeled as band 2. The BC and A_pB_p crossings are not observed, which is consistent with the configuration assignment, see Table IV. The B($M1$)/B($E2$) measurements are also consistent with these assignments and extend those made in [23].

The present work has established a new strongly coupled sequence, bands 11 and 12, which at low frequency have an alignment a few units lower than bands 7 and 8, see Fig. 12(a). Bands 11 and 12 display a gradual increase in alignment at $\hbar\omega \sim 0.35$ MeV, which is close to the BC crossing frequency, and the AB crossing is not observed. These alignment characteristics can best be explained by invoking the $AF \otimes A_pE_p(F_p)$ configuration at low frequency. Measurements of the B($M1$)/B($E2$) ratios were not possible for bands 11 and 12, due to low statistics, and the presence of stronger intensity transitions with similar energies from bands 9 and 10.

D. Towards the ultrahigh-spin regime

The behavior of ^{160}Er at high spin is intriguing. There are no clear candidates for the continuation of the yrast positive- and negative-parity normal deformed bands above $50\hbar$. The yrast band intensity drops above (50^+) with several weak transitions that could extend the structure to higher spin, Fig. 3(a). In the negative parity bands, band 1 and 2, the intensity drops dramatically above (50^-) and (49^-), respectively, and no definitive extension to high spin could be determined. The ultrahigh spin structure appears to be taken up by three regular rotational bands, labeled TSD 1, 2 and 3 in Fig. 1. Two of these bands have been reported before [20], where they were interpreted as candidates for triaxial strongly deformed structures.

In order to help understand the underlying structure of ^{160}Er up to ultrahigh spins, calculations have been performed within the framework of the configuration-dependent cranked Nilsson-Strutinsky (CNS) formalism without pairing [35, 46, 47]. Further details of these calculations can be found in Ref. [20]. Representative potential energy surfaces (PES) as a function of angular momentum with (parity, signature) $(-, 1)$ for ^{160}Er from $31\hbar$ to $61\hbar$ are displayed in Fig. 14. Similar behavior is also found for the other (π, α) configurations in ^{160}Er. The triaxiality parameter γ, used in the polar description of rotating quadrupole shapes, is defined by the Lund convention [48]. The PES of Fig. 14 indicate a wide variety of nuclear shapes that compete for yrast status as a function of angular momentum. The various minima of interest in the PES are labeled 1-5 in Fig. 14. At low spin, Fig. 14(a), the lowest-energy minimum in the PES corresponds to a well-developed prolate shape at $\gamma = 0^\circ$ and $\varepsilon_2 \sim 0.23$, labeled 1. This minimum is associated with all the normal deformed structures discussed in the previous section. As the angular momentum is increased, a minimum at an oblate (or near oblate) non-collective shape ($\gamma = 60^\circ$), labeled 4 in Fig. 14(c), develops. In addition, all the PES in Fig. 14 display two less favored minima at $\varepsilon_2 \sim 0.37$ and $\gamma \sim \pm 20^\circ$, labeled 2 and 3, corresponding to triaxial strongly deformed shapes. A more deformed triaxial minimum forms at spin values above $\sim 40\hbar$ at $\varepsilon_2 \sim 0.47$ and $\gamma \sim 22^\circ$, labeled 5 in Fig. 14(d).

1. Prolate structures

A detailed comparison between the experimentally observed near-yrast bands and their possible theoretical counterparts extracted from the CNS calculations involving configurations that originate from the deep prolate minimum, labeled 1 in Fig. 14(a), is presented in Fig. 15 up to $\sim 50\hbar$.

Both experimental, Fig. 15(a), and theoretical, Fig. 15(b), results are plotted relative to that of a rotating liquid drop based on the Lublin Strasbourg model [34, 35]. The theoretical CNS configurations are labeled $[p_1, n_1]$, where p_1 is the number of $h_{11/2}$ protons and n_1 is the number of $i_{13/2}$ neutrons involved. Fig. 15(c) provides the difference between the calculated and observed values.

The results indicate that there are three neutron configurations that compete close to the yrast line, namely, $\nu(h_{9/2}, f_{7/2})^7(i_{13/2})^3$ (both signatures) and $\nu(h_{9/2}, f_{7/2})^6(i_{13/2})^4$. These are combined with the proton configuration, $\pi(d_{5/2}, g_{7/2})^{-2}(h_{11/2})^6$, to give the lowest energy configurations, labeled $[6, 4]$, which correspond to the yrast band, and $[6, 3]$ (both signatures), which correspond to bands 1 and 2. In these bands, the low-j $N = 4$ proton occupation can be approximately described as $(d_{5/2}, g_{7/2})^{10}(d_{3/2}, s_{1/2})^2$, with equally as many particles in both signatures. Above spin $\sim 35\hbar$, the relative ordering of the calculated configurations agrees with experiment while the energy difference, Fig. 15(c), shows a small decrease. This latter fact suggests some remaining pairing correlations which decrease with angular momentum for collective bands in this spin range. In addition, the proposed high-spin CNS configurations are consistent with the active orbitals in the CSM calculations at lower spin.

The lowest energy odd spin positive parity configuration is also plotted in Fig. 15(b). This is a $[6, 4]$ configuration, but with a $(d_{5/2}, g_{7/2})^{11}(d_{3/2}, s_{1/2})^1$ occupation of the $N = 4$ proton orbitals. In this case, the odd $d_{5/2}, g_{7/2}$ proton and the $d_{3/2}, s_{1/2}$ proton both have signature $\alpha = -1/2$, leading to a total signature of $\alpha = 1$. The energy difference between this configuration and the even spin $[6, 4]$ configuration is almost constant up to $\sim 40\hbar$, which is similar in

behavior to band 5 relative to the yrast band. The high spin behavior of band 5, which at low spin is based on a γ vibration, may well be explained as this configuration.

Band 3 may correspond to the configuration with $\pi(h_{11/2})^5\nu(i_{13/2})^3$ or $[5,3]$. This configuration is much higher in energy than the $[6,4]$ band, but comes close to it at $I \sim 46$, which is similar to the behavior of band 3.

2. Termination and oblate structures

The calculations, which predict yrast prolate configurations up to spin $\sim 50\hbar$, are in good agreement with experiment, which gives confidence in the CNS model. At higher spin, competition between prolate and oblate shapes is predicted and this is demonstrated in the PES plots, see Fig. 14(c). This can be seen more clearly in Fig. 16 where the results of the CNS calculations for the lowest energy configurations are plotted, relative to that of a rotating liquid drop.

Above $I \sim 45$, oblate configurations with fewer $h_{11/2}$ protons begin to compete for yrast status. These configurations have a tendency to terminate close to the yrast line, in particular the $\pi(h_{11/2})^4$ configurations ($[4,4]$ and $[4,3]$) terminate at $I^\pi = 54^+$, 52^- and 51^-, respectively. The $[4,3]$ configuration, which terminates at $I^\pi = 51^-$, also shows another, earlier termination at $I^\pi = 47^-$ where one $f_{7/2}$ neutron is anti-aligned. In this spin region, a number of other configurations involving $(h_{11/2})^5$ protons also compete for yrast status but terminate at higher spins.

The CNS calculations do not predict a clear favored terminating state among the positive-parity even-spin states. This is consistent with the experimental observations in the yrast band, where the structure above $50\hbar$ was not clear. It is noted that the positive-parity yrast band in ^{162}Er continues its collective behavior up to the (62^+) state [49]. This is in marked contrast to the lighter erbium isotopes, ^{156,158}Er, where well-defined favored terminating states have been observed at high spin in the positive-parity yrast bands at 42^+ and 46^+, respectively [5, 50, 51]. For negative parity, the CNS calculations predict oblate terminating states at 52^- and 51^- for ^{160}Er close to the yrast line. This may well explain the drop in intensity at (50^-) and (49^-) in bands 1 and 2. At high spin in ^{160}Er, the yrast structure lies in a transitional region between well-defined yrast oblate single-particle structures, which have been observed in lighter erbium isotopes, and the continuing collective prolate structure of the heavier isotope ^{162}Er.

It is interesting to compare the intensity profiles of the lowest energy structures observed in ^{156,158,160,162}Er, see Fig. 17.

These intensity profiles are taken from this work and [50] for ^{156}Er, the data from [16] for ^{158}Er and [49] ^{162}Er. Above $30\hbar$ in ^{160}Er the intensity is almost an order of magnitude lower than in all its neighbors. The intensity collects in the lighter nuclei ^{156}Er and ^{158}Er mostly in the $(+,0)_1$ bands and collects in favored oblate states, while in the heavier nucleus ^{162}Er the intensity remains in the normal deformed prolate $(+,0)_1$ structure. The reactions used in these experiments populate these nuclei, by the $4n$ exit channel, in roughly the same excitation and spin range. The fact that the intensity in ^{160}Er is shared almost equally between three bands goes some way to explain the difference in these intensity patterns. Indeed, the negative parity bands are slightly lower in energy than the $(+,0)_1$ band above spin $30\hbar$, Fig. 11(b), which is in agreement with the calculations in Fig. 15(b). The negative parity bands in the neighboring nuclei [16, 49, 50] are much lower in intensity and higher in excitation energy, than the $(+,0)_1$ bands. The intensity in ^{160}Er above spin $\sim 50\hbar$ must, therefore, be collecting in other structures.

3. Triaxial structures

Recently, the ultrahigh-spin yrast structure of the light Er isotopes ^{157,158}Er were found to be dominated by four rotational bands with high moment of inertia [16]. These bands were compared with CNS calculations and interpreted as strongly deformed triaxial structures. Similar structures were observed in ^{159,160}Er from the present experiment [20], and the two bands TSD 1 and TSD 2 were reported. Here a third band, TSD 3, with similar characteristics was established. With the assumption that the in-band transitions are of stretched $E2$ character, the $J^{(2)}$ dynamic moment of inertia values have been extracted and all three bands in ^{160}Er are plotted in Fig. 18. The $J^{(2)}$ for TSD 3 is similar to TSD 1 and TSD 2 and exhibits a gradual decrease with rotational frequency. Therefore, TSD 3 seems to be based on a similar underlying structure and is interpreted as a third strongly deformed triaxial band.

The results of CNS calculations that predict triaxial structures occurring in ^{160}Er at high spin are reported in detail in [20]. In this work, both positive and negative-γ ($\varepsilon_2 \sim 0.37$ and $\gamma \sim \pm 20^\circ$) triaxial configurations are predicted to occur, labeled 2 and 3 in Fig. 14(a), respectively, which correspond to rotation about different axes. Positive γ ($0^\circ < \gamma < 60^\circ$) corresponds to rotation around the short axis and negative γ ($-60^\circ < \gamma < 0^\circ$) the intermediate axis, where γ is defined by the Lund convention [48]. TSD 1 and 2 were found to have better overall agreement with the characteristics of particle configurations associated with positive-γ structures, labeled 2 in Fig. 14(a), from comparisons with their extracted $J^{(2)}$ dynamic moments of inertia. In addition, the "bump" observed in these bands

at $\hbar\omega \sim 0.55$ MeV could then be attributed to an $i_{13/2}$ neutron crossing. The new band, TSD 3, does not have a clear bump at this rotational frequency. Instead the band is extended to lower frequency and a sharp rise in the $J^{(2)}$ was observed at $\hbar\omega \sim 0.4$ MeV. It is interesting to note that in the negative-γ calculations [20], a sharp bump in the $J^{(2)}$ moment was observed for various configurations at $\sim 0.4 - 0.5$ MeV, which corresponds to a crossing involving the $N_{\rm osc} = 5$ $h_{11/2}$ and $h_{9/2}, f_{7/2}$ proton orbitals. The $J^{(2)}$ of TSD 3 has a better overall agreement with the negative-γ calculations, which predict a spin range for the band from $I \sim 27$ to $I \sim 51$. However, without lifetime measurements to determine the quadrupole moment of the band, both negative and positive-γ interpretations cannot be ruled out.

Recent results obtained for the transition quadrupole moments of the TSD bands in ^{157,158}Er [52] demonstrate that the bands are strongly deformed. However, these results are not consistent with the preferred positive-γ minimum predicted by the CNS calculations, and indicated for these nuclei either a negative-γ minimum or a much more deformed positive-γ minimum. Therefore, for ^{160}Er the more deformed triaxial minimum at $\varepsilon_2 \sim 0.47$ and $\gamma \sim 22^\circ$, labeled 5 in Fig. 14(c), cannot be ruled out as a possible interpretation for these bands. The lowest configurations at $\varepsilon_2 \sim 0.47$ and $\gamma \sim 22^\circ$, are built on four neutron holes in the $N = 4$ shell, two neutron holes in the $h_{11/2}$ orbital and a neutron in the $j_{15/2}$ orbital. With increasing spin, the number of neutrons increases in the $i_{11/2}, g_{9/2}$ orbitals and decreases in the $i_{13/2}$ orbital. The proton configuration is $\pi(h_{11/2})^6(h_{9/2}, f_{7/2})^2(i_{13/2})^1$ at spins below $\sim 50\hbar$ and two proton configurations $\pi(h_{11/2})^6(h_{9/2}, f_{7/2})^2(i_{13/2})^2$ and $\pi(h_{11/2})^7(h_{9/2}, f_{7/2})^1(i_{13/2})^2$ at spins above $\sim 50\hbar$.

Fig. 19 illustrates the competition for yrast status between the lowest energy triaxial structures in ^{160}Er relative to collective prolate and single-particle oblate configurations. The configurations are labeled 1 to 5 corresponding to the minima that they originate from in the PES plots of Fig. 14. Trajectories 1 and 4 are specific [6,4] and [4,4] configurations, respectively. The configurations labeled 2, 3 and 5 are more complex, but correspond to the lowest energy states in these triaxial minima. In the spin range $\sim 40 - 65\hbar$ the positive and negative triaxial minima 2 and 3 have similar energies. Configuration 5 is the lowest of all above $\sim 60\hbar$ and is the lowest triaxial configuration above spin $\sim 55\hbar$. The observed intensity profile of the TSD bands indicates that they receive feeding from higher lying states over the entire $40 - 60\hbar$ spin range. At the present time, the data cannot identify specific configurations or triaxial shapes for the TSD bands in ^{160}Er and further information such as transition quadrupole moments from lifetime measurements is required.

V. CONCLUSION

A spectroscopic study of excited states up to ultrahigh-spin has been undertaken for the $N = 92$ nucleus ^{160}Er in order to understand the rotationally induced structural changes that occur with increasing angular momentum. The normal deformed yrast spectrum of states up to spin $\sim 50\hbar$ is dominated by a series of rotational bands, which are associated with specific quasiparticle configurations within the framework of the cranked shell model. In this work, extensions to higher and lower spins are made to many of the bands previously reported with new rotational bands and strongly coupled structures identified. At spin $\sim 50\hbar$, there is evidence for oblate terminating states coming close to the yrast line, which is in agreement with cranked Nilsson-Strutinsky calculations. This nucleus sits between the lighter ($N \leq 90$) Er isotopes, where clear yrast oblate terminating states are observed, and the heavier ($N = 94$) isotope, where normal deformed collective rotation remains yrast to higher spin. These calculations have also been used to help interpret the bands with high moments of inertia that are observed above spin $50\hbar$ as triaxial strongly deformed collective structures.

Acknowledgments

The authors acknowledge Paul Morrall for preparing the targets, and the ATLAS operations staff for assistance. This work has been supported in part by the U.S. National Science Foundation under grants No. PHY-0756474 (FSU) and PHY-0554762 (USNA), and the U.S. Department of Energy, Office of Nuclear Physics, under contracts No. DE-AC02-06CH11357 (ANL), DE-FG02-94ER40834 (UMD), DE-AC02-05CH11231 (LBL), and DE-FG02-96ER40983(UTK), the United Kingdom Science and Technology Facilities Council, the Swedish Science Research Council, and by the State of Florida.

[1] A. Johnson, H. Ryde, and J. Sztarkier, Phys. Lett. B **34**, 605 (1971).
[2] F. S. Stephens and R. S. Simon, Nucl. Phys. A **183**, 257 (1972).
[3] W. Nazarewicz, J. Dudek, R. Bengtsson, T. Bengtsson, and I. Ragnarsson, Nucl. Phys. A **435**, 397 (1985).

[4] S. Cwiok, J. Dudek, W. Nazarewicz, W. Skalski, and T. Werner, Comp. Phys. Comm. **46**, 379 (1987).
[5] P. O. Tjøm, R. M. Diamond, J. C. Bacelar, E. M. Beck, M. A. Deleplanque, J. E. Draper, and F. S. Stephens, Phys. Rev. Lett. **55**, 2405 (1985).
[6] S. J. Gale, J. Simpson, M. A. Riley, J. F. Sharpey-Schafer, E. S. Paul, M. A. Bentley, A. M. Bruce, R. Chapman, R. M. Clark, S. Clarke, et al., J. Phys. G. **21**, 193 (1995).
[7] F. S. Stephens, M. A. Deleplanque, R. M. Diamond, A. O. Macchiavelli, and J. E. Draper, Phys. Rev. Lett. **54**, 2584 (1985).
[8] H. W. Cranmer-Gordon, P. D. Forsyth, D. V. Elenkov, D. Howe, J. F. Sharpey-Schafer, M. A. Riley, G. Sletten, J. Simpson, I. Ragnarsson, Z. Xing, et al., Nucl. Phys. A **465**, 506 (1987).
[9] H. Emling, I. Ahmad, P. J. Daly, B. K. Dichter, M. Drigert, U. Garg, Z. W. Grabowski, R. Holzmann, R. V. F. Janssens, T. L. Khoo, et al., Phys. Lett. B **217**, 33 (1989).
[10] J. D. Morrison, J. F. Sharpey-Schafer, M. A. Bentley, H. W. Cranmer-Gordon, P. Fallon, P. D. Forsyth, D. Howe, A. R. Mokhtar, M. A. Riley, and J. Simpson, Europhys. Lett. **6**, 493 (1988).
[11] C. Baktash, Y. Schutz, I. Y. Lee, F. K. McGowan, N. R. Johnson, M. L. Halbert, D. C. Hensley, M. P. Fewell, L. Courtney, A. J. Larabee, et al., Phys. Rev. Lett. **54**, 978 (1985).
[12] T. Byrski, F. A. Beck, J. C. Merdinger, A. Nourreddine, H. W. Cranmer-Gordon, D. V. Elenkov, P. D. Forsyth, D. Howe, M. A. Riley, J. F. Sharpey-Schafer, et al., Nucl. Phys. A **474**, 193 (1987).
[13] M. A. Riley, J. D. Garrett, J. F. Sharpey-Schafer, and J. Simpson, Phys. Lett. B **177**, 15 (1986).
[14] I. Ragnarsson, Z. Xing, T. Bengtsson, and M. A. Riley, Phys. Scr. **34**, 651 (1986).
[15] J. Burde, E. L. Dines, S. Shih, R. M. Diamond, J. E. Draper, K. H. Lindenberger, C. Schück, and F. S. Stephens, Phys. Rev. Lett. **48**, 530 (1982).
[16] E. S. Paul, P. J. Twin, A. O. Evans, A. Pipidis, M. A. Riley, J. Simpson, D. E. Appelbe, D. B. Campbell, P. T. W. Choy, R. M. Clark, et al., Phys. Rev. Lett. **98**, 012501 (2007).
[17] A. Aguilar, D. B. Campbell, K. Chandler, A. Pipidis, M. A. Riley, C. Teal, J. Simpson, D. J. Hartley, F. G. Kondev, R. M. Clark, et al., Phys. Rev. C **77**, 021302 (2008).
[18] C. Teal, K. Lagergren, A. Aguilar, M. A. Riley, J. Simpson, M. P. Carpenter, U. Garg, D. J. Hartley, R. V. F. Janssens, D. T. Joss, et al., Phys. Rev. C **78**, 017305 (2008).
[19] N. S. Pattabiraman, Y. Gu, S. Frauendorf, U. Garg, T. Li, B. K. Nayak, X. Wang, S. Zhu, R. V. F. Janssens, R. S. Chakrawarthy, et al., Phys. Lett. **B647**, 243 (2007).
[20] J. Ollier, J. Simpson, X. Wang, M. A. Riley, A. Aguilar, C. Teal, E. S. Paul, P. J. Nolan, M. Petri, S. V. Rigby, et al., Phys. Rev. C **80**, 064322 (2009).
[21] J. Simpson, M. A. Riley, J. R. Cresswell, D. V. Elenkov, P. D. Forsyth, G. B. Hagemann, D. Howe, B. M. Nyakó, S. Ogaza, J. C. Lisle, et al., J. Phys. G **13**, 847 (1987).
[22] K. Dusling, N. Pietralla, G. Rainovski, T. Ahn, B. Bochev, A. Costin, T. Koike, T. C. Li, A. Linnemann, S. Pontillo, et al., Phys. Rev. C **73**, 014317 (2006).
[23] J. Simpson, M. Riley, R. Laird, D. Hartley, F. Kondev, J. Sweeney, A. Wilson, S. Gale, M. Bentley, A. Bruce, et al., Eur. Phys. J. A **1**, 267 (1998).
[24] J. Simpson, M. A. Riley, A. N. James, A. R. Mokhtar, H. W. Cranmer-Gorden, P. D. Forsyth, A. J. Kirwan, D. Howe, J. D. Morrison, and J. F. Sharpey-Schafer, J. Phys. G **13**, L235 (1987).
[25] F. G. Kondev, M. A. Riley, J. Simpson, R. V. F. Janssens, A. V. Afanasjev, I. Ragnarsson, T. B. Brown, D. J. Hartley, M. P. Carpenter, P. Fallon, et al., J. Phys. G **25**, 897 (1999).
[26] I. Y. Lee, Nucl. Phys. **A520**, 641c (1990).
[27] R. V. F. Janssens and F. S. Stephens, Nucl. Phys. News **6**, 9 (1996).
[28] D. C. Radford, Nucl. Instrum. Methods Phys. Res., Sect. A **361**, 297 (1995).
[29] D. C. Radford, M. Cromaz, and C. J. Beyer, in *Proceedings of the Nuclear Structure '98 Conference, Gatlinburg, 1998,* edited by C. Baktash, p. 570 (American Institute of Physics, College Park, MD, 1999).
[30] C. Beausang, D. Prevost, M. Bergstrom, G. deFrance, B. Haas, J. Lisle, C. Theisen, J. Timár, P. Twin, and J. Wilson, Nucl. Instrum. Methods Phys. Res. A **364**, 560 (1995).
[31] L. P. Ekström and A. Nordlund, Nucl. Instrum. Methods Phys. Res. A **313**, 421 (1992).
[32] J. P. Sweeney, R. Chapman, S. Araddad, J. Copnell, A. Fitzpatrick, S. J. Freeman, F. Liden, J. C. Lisle, A. G. Smith, D. M. Thompson, et al., Daresbury Lab. Ann. Rept., Appendix, p. 38 (1993).
[33] R. Bengtsson, S. Frauendorf, and F.-R. May, At. Data and Nucl. Data Tables **35**, 15 (1986).
[34] K. Pomorski and J. Dudek, Phys. Rev. C **67**, 044316 (2003).
[35] B. G. Carlsson and I. Ragnarsson, Phys. Rev. C **74**, 011302 (2006).
[36] N. Rowley, J. Ollier, and J. Simpson, Phys. Rev. C **80**, 024323 (2009).
[37] S. M. Harris, Phys. Rev. Lett. **13**, 663 (1964).
[38] S. M. Harris, Phys. Rev. **138**, B509 (1965).
[39] B. Singh, A. Kogan, and S. K. Mark, Phys. Rev. C **28**, 2118 (1983).
[40] M. A. Riley, J. Simpson, R. Aryaeinejad, J. R. Cresswell, P. D. Forsyth, D. Howe, P. J. Nolan, B. M. Nyakó, J. F. Sharpey-Schafer, P. J. Twin, et al., Phys. Lett. B **135**, 275 (1984).
[41] A. Nordlund, R. Bengtsson, P. Ekström, M. Bergström, A. Brockstedt, H. Carlsson, H. Ryde, Y. Sun, A. Atac, G. B. Hagemann, et al., Nucl. Phys. A **591**, 117 (1995).
[42] D. R. Jensen, J. Domscheit, G. B. Hagemann, M. Bergström, B. Herskind, B. S. Nielsen, G. Sletten, P. G. Varmette, S. Törmänen, H. Hübel, et al., Eur. Phys. J. A **8**, 165 (2000).

[43] E. S. Paul, P. Bednarczyk, A. J. Boston, C. J. Chiara, C. Foin, D. B. Fossan, J. Genevey, A. Gizon, J. Gizon, D. G. Jenkins, et al., Nucl. Phys. A **676**, 32 (2000).
[44] F. Dönau and S. Frauendorf, *Proc. Conf. on High Angular Momentum Properties of Nuclei, Oak Ridge, ed N R Johnson(New York: Harwood)* p. p143 (1982).
[45] F. Dönau, Nucl. Phys. A **471**, 469 (1987).
[46] A. V. Afanasjev, D. B. Fossan, G. J. Lane, and I. Ragnarsson, Physics Reports **322**, 1 (1999), ISSN 0370-1573.
[47] T. Bengtsson and I. Ragnarsson, Nucl. Phys. **A436**, 14 (1985).
[48] G. Andersson, S. E. Larsson, G. Leander, P. Möller, S. G. Nilsson, I. Ragnarsson, S. Åberg, R. Bengtsson, J. Dudek, B. Nerlo-Pomorska, et al., Nucl. Phys. **A268**, 205 (1976).
[49] J. Simpson, A. P. Bagshaw, A. Pipidis, M. A. Riley, M. A. Bentley, D. M. Cullen, P. J. Dagnall, G. B. Hagemann, S. L. King, R. W. Laird, et al., Phys. Rev. C **62**, 024321 (2000).
[50] E. S. Paul, S. V. Rigby, M. A. Riley, J. Simpson, D. E. Appelbe, D. B. Campbell, P. T. W. Choy, R. M. Clark, M. Cromaz, A. O. Evans, et al., Phys. Rev. C **79**, 044324 (2009).
[51] J. Simpson, M. A. Riley, S. J. Gale, J. F. Sharpey-Schafer, M. A. Bentley, A. M. Bruce, R. Chapman, R. M. Clark, S. Clarke, J. Copnell, et al., Phys. Lett. B **327**, 187 (1994).
[52] X. Wang, M. A. Riley, J. Simpson, E. S. Paul, J. Ollier, R. V. Janssens, A. D. Ayangeakaa, H. C. Boston, M. P. Carpenter, C. J. Chiara, et al., Phys. Rev. Lett. submitted (2010).

Figures

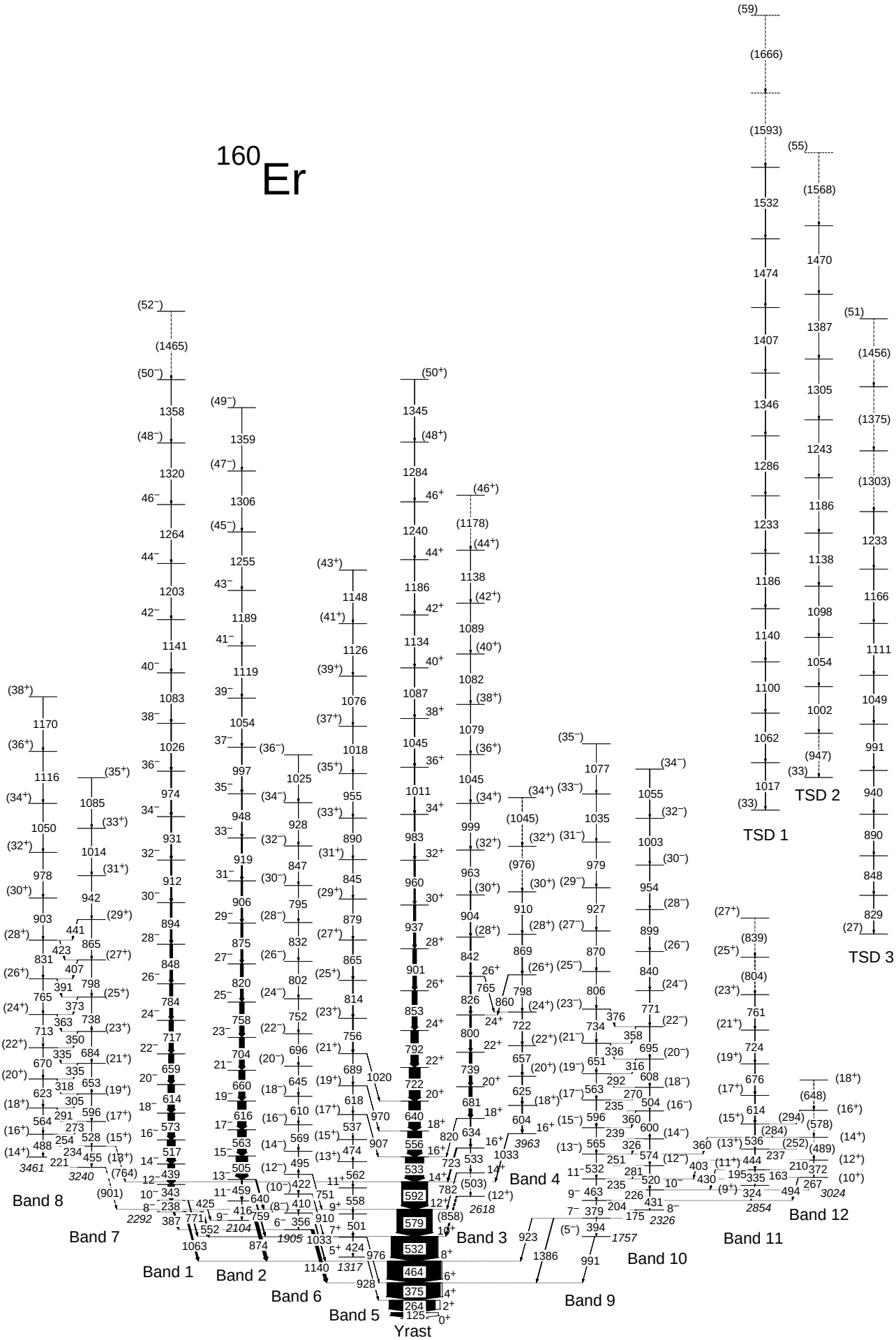
160Er
Band 1
Band 2
Band 3
Band 4
Band 5
Band 6
Band 7
Band 8
Band 9
Band 10
Band 11
Band 12
TSD 1
TSD 2
TSD 3
Yrast

FIG. 1: The level scheme for ^{160}Er constructed from the present work. Energies are given in keV and the width of the arrows is proportional to the relative intensity of the transitions. Spin assignments and excitation energy of the bands labeled TSD 1, 2 and 3 are based on comparisons with results from CNS calculations, see text as well as Ref. [20].

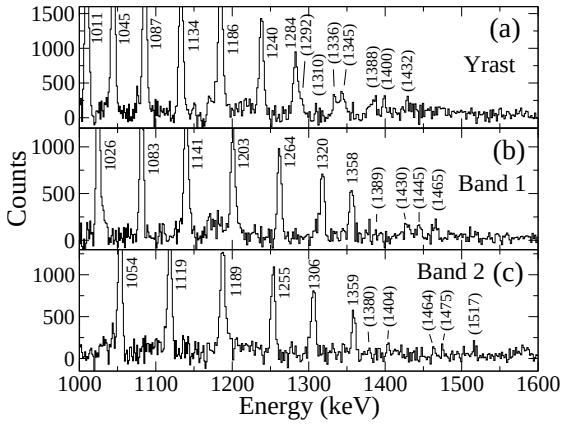

FIG. 2: Background subtracted γ-ray spectra produced with sums of triple gates from the E_γ^4 hypercube for (a) the positive-parity yrast band, (b) band 1 and (c) band 2 in ^{160}Er. Photopeaks labeled with parentheses are tentative, see text for details.

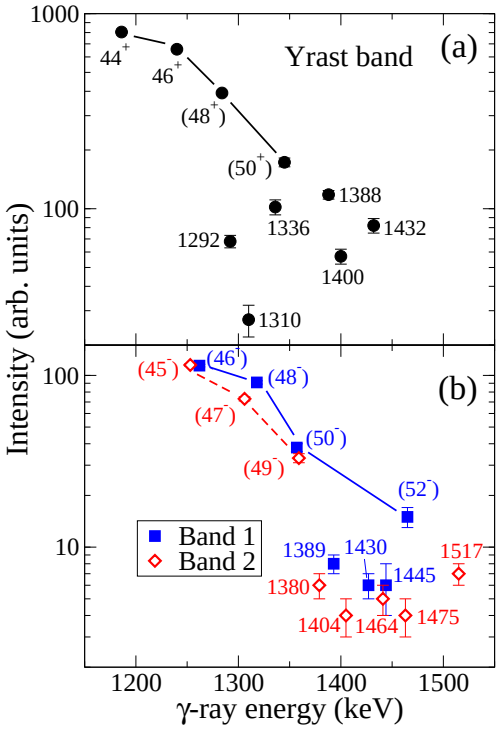

FIG. 3: (Color online) Intensity profiles for the top of the positive-parity yrast band (a) and the negative parity bands 1 and 2 (b), relative to sums of triple coincidences set in the E_γ^4 hypercube up to the $I^\pi = 42^+$ state for the yrast band and the 44^- and 43^- levels for bands 1 and 2, respectively. Transitions that are not fixed in the level scheme are denoted by their energy, see text for details.

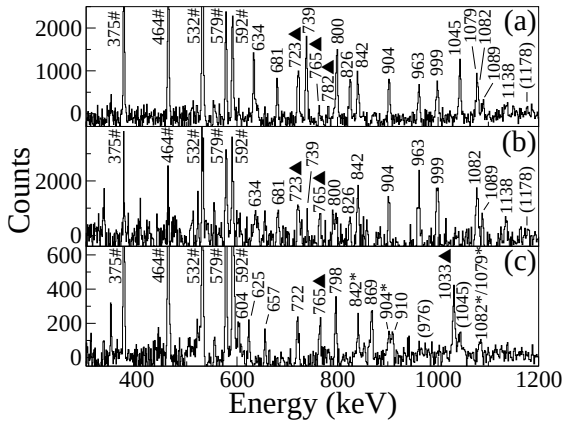

FIG. 4: Background subtracted γ-ray spectra for (a) band 3 produced with a sum of triple gates, (b) band 3 produced with a double gate set on the 1045 and 1079 keV transitions, and (c) band 4 produced with a sum of triple gates involving the first four transitions up to the decay of the $I^{\pi} = (24^{+})$ state. Photopeaks corresponding to linking transitions are labeled with triangles, photopeaks that correspond to transitions within the yrast band are labeled ♯, photopeaks that are labeled "$*$" in (c) correspond to transitions associated with band 3 (see text for details) and photopeaks labeled with parentheses are tentative.

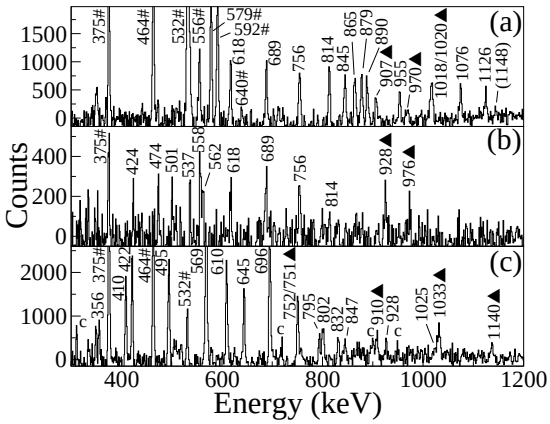

FIG. 5: Background subtracted γ-ray spectra for (a) band 5 produced with a sum of triple gates set above its (17^+) level, (b) band 5 produced with a sum of triple gates set below its (17^+) level, and (c) band 6 produced with a sum of triple gates. Photopeaks corresponding to linking transitions are labeled with triangles, photopeaks that correspond to transitions within the yrast band are labeled ♯, photopeaks labeled with parentheses are tentative and photopeaks labeled "c" are contaminant peaks of unknown origin brought in by the gating process.

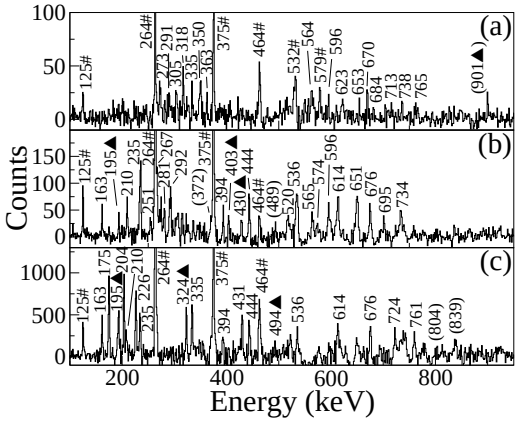

FIG. 6: Background subtracted γ-ray spectra characteristic for transitions from (a) bands 7 and 8 produced with a triple gate at 221, 234 and 255 keV, (b) bands 9, 10, 11 and 12 produced with a triple gate at 175, 204 and 227 keV and (c) bands 9, 10, 11 and 12 produced with sums of triple gates set at 444, 536, 614 and 676 keV. Photopeaks corresponding to linking transitions are labeled with triangles, photopeaks that correspond to transitions within the yrast band are labeled ♯ and photopeaks labeled with parentheses are tentative.

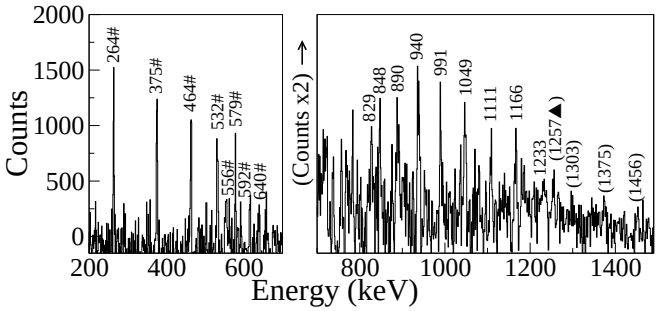

FIG. 7: Background subtracted γ-ray spectrum produced with a sum of triple gates set on all the transitions associated with band TSD 3 up to the 1233 keV γ ray. Photopeaks labeled ♯ correspond to transitions within the yrast band, the photopeak labeled with a triangle is a possible linking transition and photopeaks labeled with parentheses are tentative.

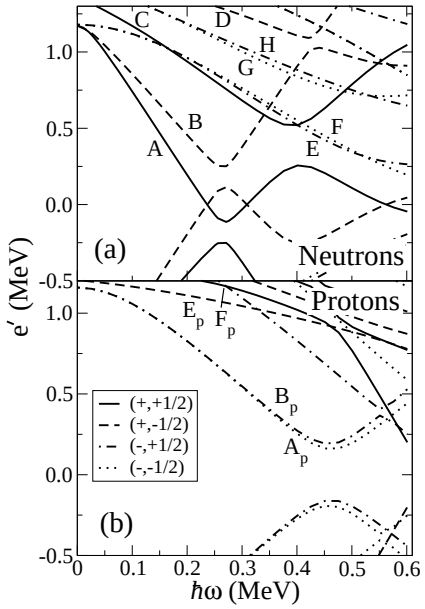

FIG. 8: The results of CSM calculations for ^{160}Er (a) neutrons and (b) protons. The deformation parameters used were $\beta_2 = 0.253$, $\beta_4 = 0.040$ and $\gamma = 0.0^0$, and with Δ_n and $\Delta_p = 1.14$ MeV. The quasiparticle labeling is given in Table III and the legend denotes the parity and signature as (π, α) of the orbitals.

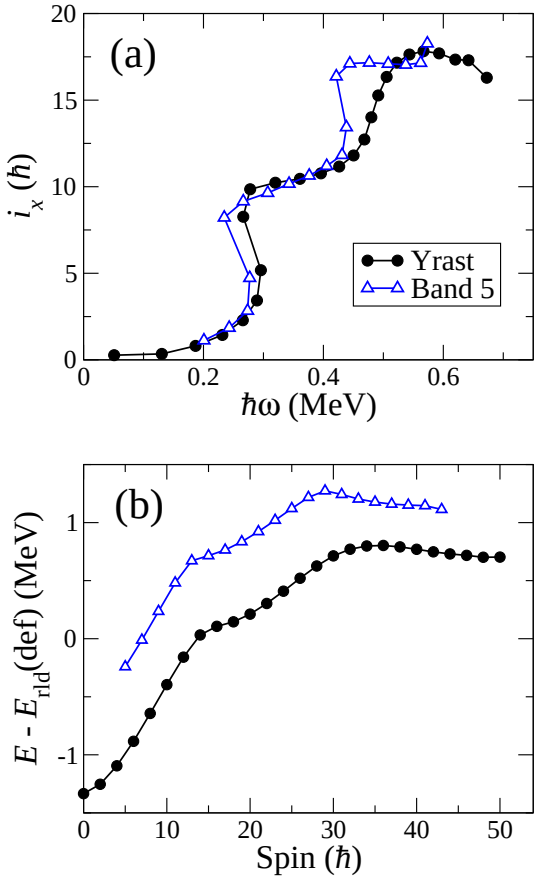

FIG. 9: (Color online) (a) The aligned angular momentum (alignment) as a function of rotational frequency for the yrast band and band 5 ($K = 2$). (b) Energy relative to a rotating liquid drop as a function of spin for these bands.

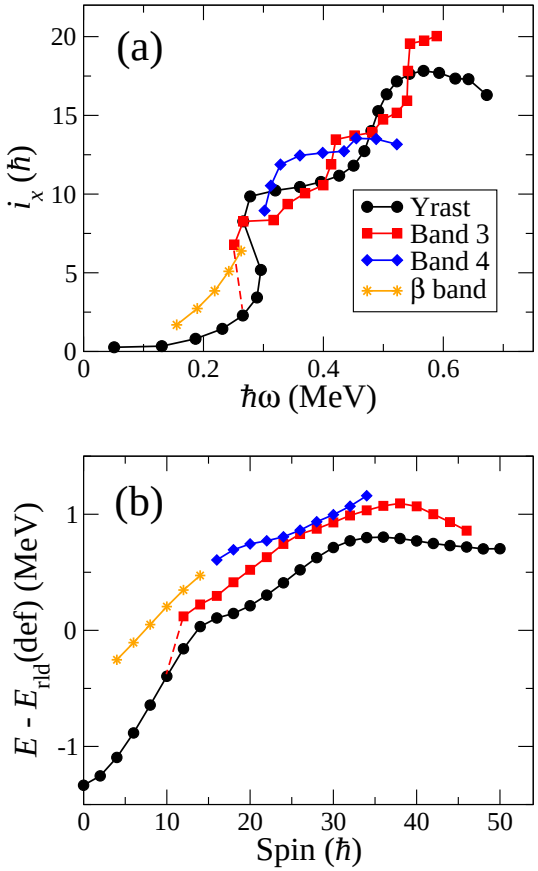

FIG. 10: (Color online) (a) The aligned angular momentum (alignment) as a function of rotational frequency for the yrast band, band 3 and 4 and the β band observed by [22, 39]. (b) Energy relative to a rotating liquid drop as a function of spin for these bands.

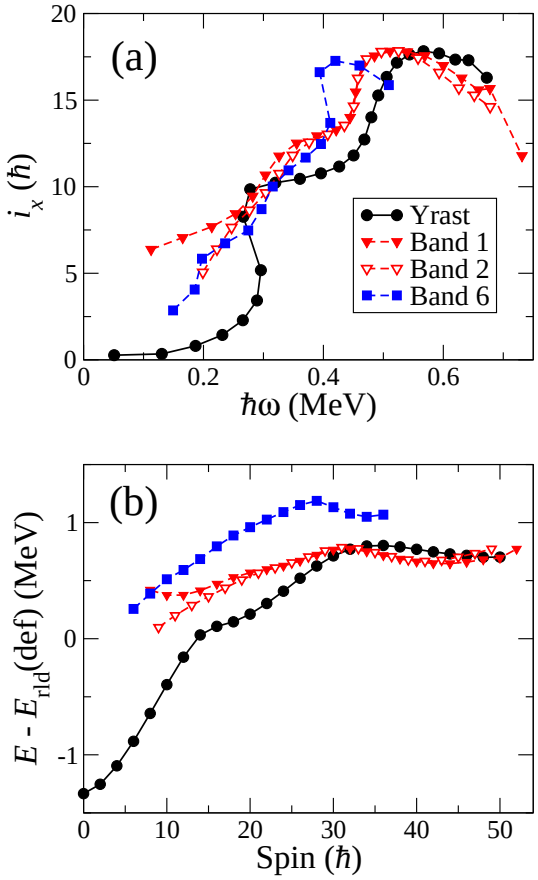

FIG. 11: (Color online) (a) The aligned angular momentum (alignment) as a function of rotational frequency for the yrast band and the negative parity bands 1, 2 and 6. (b) Energy relative to a rotating liquid drop as a function of spin for these bands.

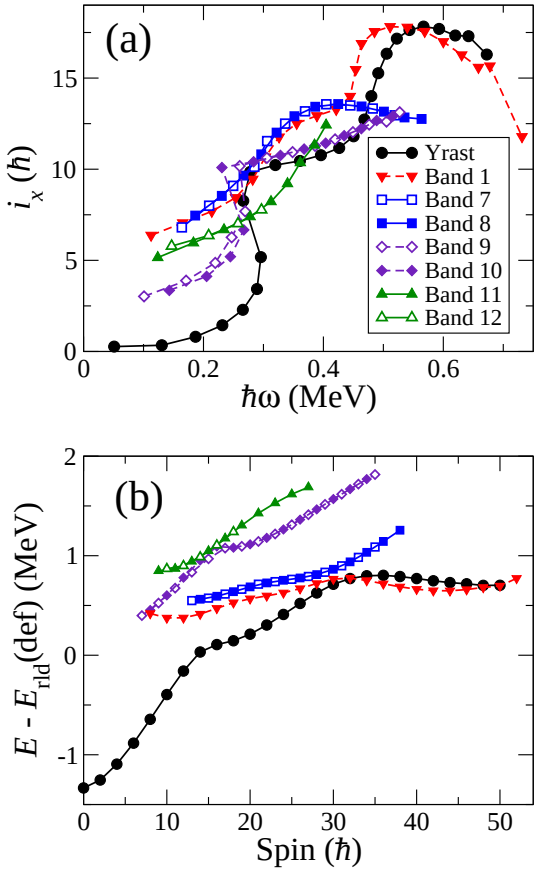

FIG. 12: (Color online) (a) The aligned angular momentum (alignment) as a function of rotational frequency for the strongly coupled bands (bands 7-12). The yrast band and band 1 are plotted for comparison. (b) Energy relative to a rotating liquid drop as a function of spin for these bands.

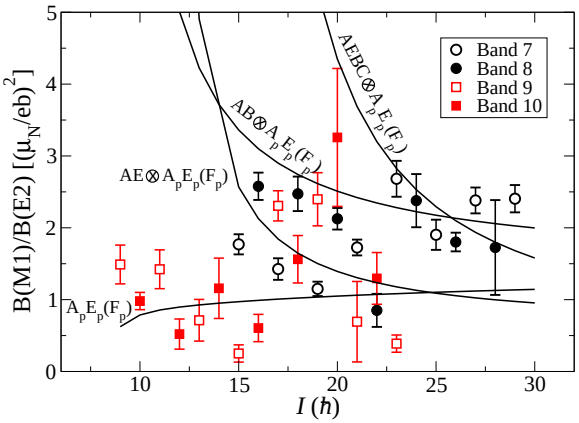

FIG. 13: (Color online) Experimental B(M1)/B(E2) ratios as a function of spin. The solid lines represent the theoretical predictions for the proposed configurations using the geometric model [44, 45].

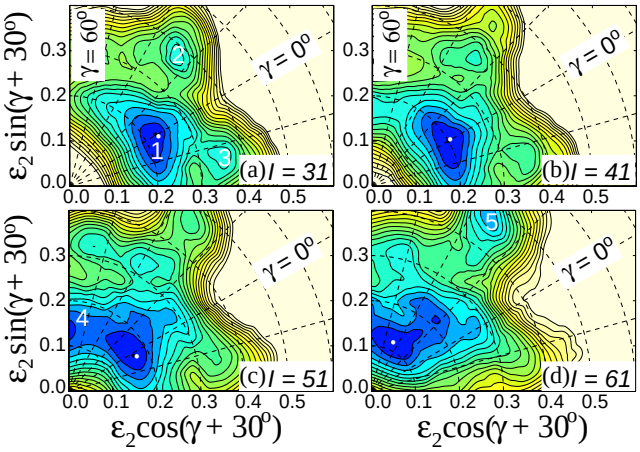

FIG. 14: Calculated potential-energy surfaces versus quadrupole deformation ε_2 and the triaxiality parameter γ for ^{160}Er with $(\pi, \alpha) = (-, 1)$ at spins $I = 31$, 41, 51 and 61 labeled (a)-(d), respectively. Contour lines are separated by 0.25 MeV and the γ plane marked at 15° intervals. Dark regions represent low energy with absolute minima labeled with a white dot. Individual minima labeled 1-5 are discussed in the text.

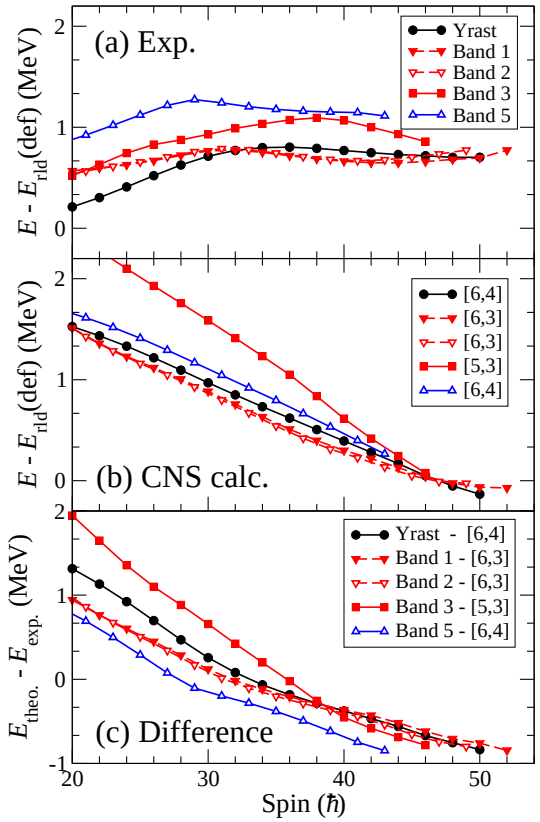

FIG. 15: (Color online) (a) Energy relative to a rotating liquid drop [34, 35] as a function of spin for the near yrast bands observed above $20\hbar$, (b) Calculated excitation energies relative to a rotating liquid drop as a function of spin for the lowest energy states based on collective prolate structures, see text for details of configuration labeling, and (c) the difference between (a) and (b). Solid lines correspond to positive parity configurations and broken lines to negative parity ones. Similarly, solid symbols correspond to positive signature and open symbols to negative signature.

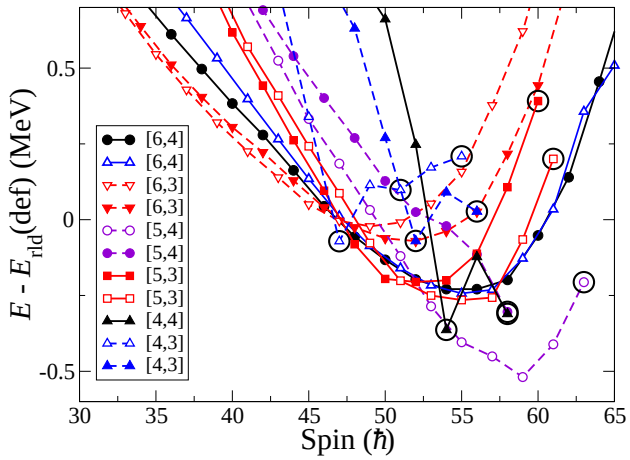

FIG. 16: (Color online) Calculated excitation energies relative to a rotating liquid drop [34, 35] as a function of spin for the lowest energy states based on collective prolate and single-particle oblate configurations, see text for details of configuration labeling. The convention style for the lines and symbols is as given in Fig. 15. The large open circles indicate oblate non-collective band terminating states.

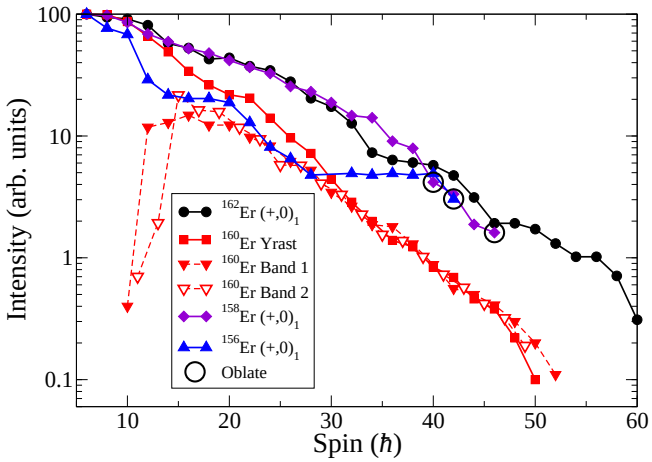

FIG. 17: (Color online) Intensity profiles for the yrast, band 1 and band 2 in ^{160}Er, from the present work. Also plotted are the intensities in the $(+,0)_1$ band for ^{158}Er (from the data of [16]), and ^{156}Er [50] and ^{162}Er [49], plotted relative to their $6^+ \rightarrow 4^+$ yrast transition intensity.

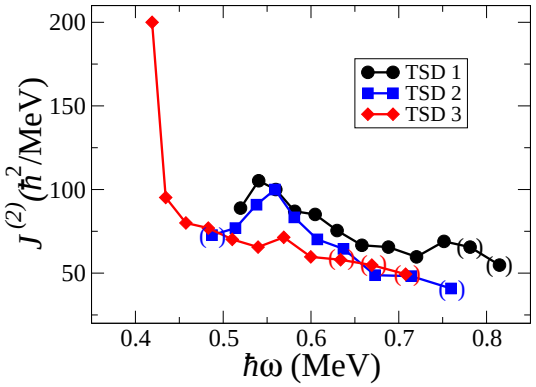

FIG. 18: (Color online) The dynamic moment of inertia $J^{(2)}$ as a function of rotational frequency for the three proposed TSD bands in ^{160}Er. The parentheses are associated with tentative transitions.

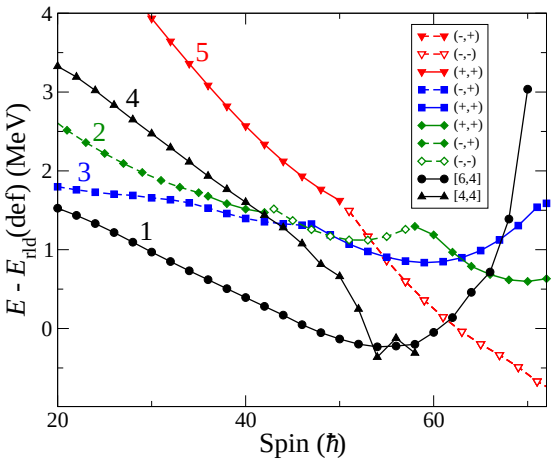

FIG. 19: (Color online) Calculated excitation energies relative to a rotating liquid drop [34, 35] as a function of spin for the lowest energy states based on collective triaxial configurations, see text for details, and prolate and single-particle oblate configurations. The convention style for the lines and symbols is as given in Fig. 15. The configuration labels 1 to 5 correspond to the minima in the PES plots of Fig. 14.

Tables

TABLE I: Energies E_γ, intensities I_γ, angular intensity ratios R and spin-parity assignments for the transitions observed in ^{160}Er from the present work. The γ-ray energies are estimated to be accurate to ± 0.3 keV for the strong transitions ($I_\gamma > 10$), rising to ± 0.6 keV for the weaker transitions. The intensity measurements have been normalized to the 375 keV ($6^+ \rightarrow 4^+$) yrast transition with a value of 100. The bands are labeled in order of the scheme shown in Fig. 1 and excitation energy E_x.

Band	E_γ (keV)	I_γ	R	Multipolarity	$I^\pi_{\rm initial}$	$I^\pi_{\rm final}$
Yrast						
	125.4			$E2^a$	2^+	0^+
	263.8	>100	0.86(6)	$E2$	4^+	2^+
	375.4	100	0.87(7)	$E2$	6^+	4^+
	463.8	99.8(3.2)	0.92(6)	$E2$	8^+	6^+
	531.7	87.1(2.6)	1.21(9)	$E2$	10^+	8^+
	578.9	65.9(2.1)	1.11(11)	$E2$	12^+	10^+
	591.9	48.6(1.6)	1.15(10)	$E2$	14^+	12^+
	533.3	34.4(1.0)	1.21(9)	$E2$	16^+	14^+
	555.5	26.3(8)	1.12(12)	$E2$	18^+	16^+
	640.0	21.9(8)	0.98(12)	$E2$	20^+	18^+
	721.9	20.5(5)	1.16(16)	$E2$	22^+	20^+
	792.4	14.0(3)	1.23(26)	$E2$	24^+	22^+
	852.5	9.63(26)	1.11(17)	$E2$	26^+	24^+
	901.4	7.19(26)	1.10(27)	$E2$	28^+	26^+
	936.6	4.43(13)	1.20(5)	$E2$	30^+	28^+
	960.0	2.86(7)	1.22(38)	$E2$	32^+	30^+
	983.2	1.99(5)	1.22(4)	$E2$	34^+	32^+
	1011.2	1.39(4)		$E2^a$	36^+	34^+
	1045.4	1.23(4)		$E2^a$	38^+	36^+
	1087.0	0.84(3)	1.47(11)	$E2$	40^+	38^+
	1134.3	0.69(2)	1.45(51)	$E2$	42^+	40^+
	1186.3	0.46(2)	1.24(51)	$E2$	44^+	42^+
	1239.8	0.38(2)	1.43(11)	$E2$	46^+	44^+
	1284.3	0.22(1)			(48^+)	46^+
	1344.8	0.10(1)			(50^+)	(48^+)
	(1388)	0.07(1)			$>(50^+)$	
	(1336)	0.06(1)			$>(50^+)$	
	(1292)	0.04(1)			$>(50^+)$	
	(1400)	0.03(1)			$>(50^+)$	
	(1432)	0.05(1)			$>(50^+)$	
	(1310)	0.01(1)			$>(50^+)$	
Band 1						
1 $\rightarrow$yrast	1062.9	3.08(9)	1.08(29)	$E1^a$	8^-	8^+
1 $\rightarrow$5	551.8	5.91(18)	0.70(23)	E1	8^-	7^+
1 $\rightarrow$6	387.2	2.89(8)	0.93(12)	$E2$	8^-	6^-
	238.2	0.40(1)	0.86(8)	$E2$	10^-	8^-
1 $\rightarrow$yrast	770.7	1.57(4)	1.07(7)	$E1$	10^-	10^+
1 $\rightarrow$ 2	424.6	0.60(2)	0.99(4)	$M1/E2$	10^-	9^-
	343.1	11.81(36)	1.00(5)	$E2$	12^-	10^-
	439.0	12.91(39)	1.15(5)	$E2$	14^-	12^-
	517.0	14.82(47)	0.97(4)	$E2$	16^-	14^-
	572.8	12.28(37)	1.11(6)	$E2$	18^-	16^-
	613.9	12.29(37)	1.21(7)	$E2$	20^-	18^-
	658.8	9.77(29)	1.08(6)	$E2$	22^-	20^-
	716.7	8.27(25)	1.18(7)	$E2$	24^-	22^-
	784.0	6.18(19)	1.34(8)	$E2$	26^-	24^-
	847.7	5.23(16)	1.13(6)	$E2$	28^-	26^-

TABLE I: (continued)

Band	E_γ (keV)	I_γ	R	Multipolarity	$I^\pi_{\rm initial}$	$I^\pi_{\rm final}$
	893.8	3.45(10)	1.05(6)	$E2$	30^-	28^-
	912.3	2.65(8)	1.25(8)	$E2$	32^-	30^-
	931.4	1.87(6)	1.16(8)	$E2$	34^-	32^-
	973.6	1.80(6)	1.11(8)	$E2$	36^-	34^-
	1026.4	1.30(4)	1.34(11)	$E2$	38^-	36^-
	1083.3	0.88(3)	1.21(11)	$E2$	40^-	38^-
	1141.4	0.56(2)	1.25(12)	$E2$	42^-	40^-
	1203.1	0.50(2)	1.04(18)	$E2$	44^-	42^-
	1263.7	0.41(1)	1.10(20)	$E2$	46^-	44^-
	1320.0	0.30(1)	1.31(43)	$(E2)$	(48^-)	46^-
	1358.1	0.20(1)	1.19(47)	$(E2)$	(50^-)	(48^-)
	(1465)	0.11(1)			(52^-)	(50^-)
Band 2						
2 →yrast	874.3	5.93(21)	0.56(11)	$E1$	9^-	8^+
	415.7	0.70(2)	1.29(58)	$E2^a$	11^-	9^-
2 →yrast	759.1	1.73(5)	0.91(6)	$E1^a$	11^-	10^+
	459.4	1.93(6)	1.17(9)	$E2$	13^-	11^-
2 →yrast	639.9	2.14(6)	0.64(9)	$E1$	13^-	12^+
	504.5	21.63(65)	1.17(7)	$E2$	15^-	13^-
	562.5	16.30(49)	1.16(8)	$E2$	17^-	15^-
	615.9	15.78(48)	1.25(12)	$E2$	19^-	17^-
	660.3	11.72(35)	1.16(11)	$E2$	21^-	19^-
	704.1	9.42(28)	1.14(10)	$E2$	23^-	21^-
	757.6	5.78(26)	0.91(6)	$E2$	25^-	23^-
	819.5	5.72(17)	1.23(12)	$E2$	27^-	25^-
	874.6	4.08(12)	1.12(12)	$E2$	29^-	27^-
	905.5	3.30(10)	1.09(11)	$E2$	31^-	29^-
	918.9	2.27(7)	1.25(14)	$E2$	33^-	31^-
	948.3	1.55(5)	1.33(16)	$E2$	35^-	33^-
	996.6	1.38(4)	1.24(15)	$E2$	37^-	35^-
	1054.6	1.02(3)	1.44(28)	$E2$	39^-	37^-
	1119.0	0.73(2)	1.00(19)	$E2$	41^-	39^-
	1189.4	0.57(2)	1.50(35)	$E2$	43^-	41^-
	1254.5	0.42(1)	1.37(41)	$(E2)$	(45^-)	43^-
	1306.4	0.32(1)	1.88(77)	$(E2)$	(47^-)	(45^-)
	1358.8	0.19(1)	0.92(47)	$(E2)$	(49^-)	(47^-)
Band 3						
3 →yrast	782.4	5.69	0.90(22)	$E2^a$	14^+	12^+
	533.4	0.67(3)		$E2^a$	16^+	14^+
3 →yrast	723.2	2.03(12)	1.28(16)	$E2$	16^+	14^+
	633.9	1.62(5)	1.45(35)	$E2$	18^+	16^+
3 →yrast	819.6	0.06(1)			18^+	16^+
	681.0	6.23(19)	1.70(29)	$E2$	20^+	18^+
	739.3	5.15(16)	1.04(12)	$E2$	22^+	20^+
	800.3	3.46(10)	0.98(19)	$E2$	24^+	22^+
	826.3	2.52(8)	0.93(17)	$E2$	26^+	24^+
3 → 4	764.7	0.30(1)			26^+	(24^+)
	841.8	2.12(7)	0.70(17)	$(E2)$	(28^+)	(26^+)
	904.4	1.26(4)	1.00(25)	$(E2)$	(30^+)	(28^+)
	962.8	0.56(2)	1.13(54)	$(E2)$	(32^+)	(30^+)
	999.2	0.51(2)	1.16(47)	$(E2)$	(34^+)	(32^+)
	1045.0	0.46(2)	0.88(26)	$(E2)$	(36^+)	(34^+)
	1078.6	0.34(1)	0.80(34)	$(E2)$	(38^+)	(36^+)
	1081.5	0.11(1)			(40^+)	(38^+)
	1089.0	0.08(1)			(42^+)	(40^+)
	1137.8	0.08(1)			(44^+)	(42^+)
	(1178)	0.08(1)			(46^+)	(44^+)
Band 4						
4 →yrast	1033.0	0.86(3)	1.10(29)	$E2$	16^+	14^+

TABLE I: (continued)

Band	E_γ (keV)	I_γ	R	Multipolarity	$I^\pi_{\rm initial}$	$I^\pi_{\rm final}$
	604.1	1.52(9)			(18^+)	16^+
	624.5	1.50(7)	1.04(9)	$E2$	(20^+)	(18^+)
	656.9	1.27(7)			(22^+)	(20^+)
	721.7	1.13(6)	1.30(8)	$E2$	(24^+)	(22^+)
	798.3	0.54(5)	1.12(21)	$E2$	(26^+)	(24^+)
$4 \rightarrow 3$	859.7	0.77(2)			(26^+)	(24^+)
	869.0	1.27(5)			(28^+)	(26^+)
	910.3	0.75(3)	1.11(17)	$E2$	(30^+)	(28^+)
	(976)				(32^+)	(30^+)
	(1045)				(34^+)	(32^+)
Band 5						
5 →yrast	927.8	0.36(3)		$M1/E2^a$	5^+	4^+
	424.3	0.15(1)		$E2^a$	7^+	5^+
5 →yrast	976.4	0.05(1)		$M1/E2^a$	7^+	6^+
	501.4	1.04(4)		$E2^a$	9^+	7^+
	557.8	0.33(2)		$E2^a$	11^+	9^+
	562.3	0.26(2)			(13^+)	11^+
	473.8	0.13(1)			(15^+)	(13^+)
	536.6	0.09(1)			(17^+)	(15^+)
5 →yrast	907.4	0.32(1)			(17^+)	(16^+)
	618.0	0.38(7)			(19^+)	(17^+)
5 →yrast	970.1	0.28(2)			(19^+)	(18^+)
	688.7	0.59(2)			(21^+)	(19^+)
5 →yrast	1020.2	0.24(2)			(21^+)	(20^+)
	756.1	1.69(6)			(23^+)	(21^+)
	813.9	1.50(4)			(25^+)	(23^+)
	864.8	1.46(4)			(27^+)	(25^+)
	879.2	0.65(2)			(29^+)	(27^+)
	845.3	0.38(2)			(31^+)	(29^+)
	889.9	0.24(1)			(33^+)	(31^+)
	954.7	0.19(1)			(35^+)	(33^+)
	1017.6	0.14(1)			(37^+)	(35^+)
	1075.9	0.14(1)			(39^+)	(37^+)
	1126.2	0.13(1)			(41^+)	(39^+)
	1148.0	0.06(1)			(43^+)	(41^+)
Band 6						
6 →yrast	1139.7	5.54(21)	1.62(27)	$E2$	6^-	6^+
	356.4	0.55(2)			(8^-)	6^-
6 →yrast	1032.8	1.29(4)			(8^-)	8^+
	409.5	0.94(3)	1.17(26)	$E2$	(10^-)	(8^-)
6 →yrast	910.2	0.21(2)	1.10(8)	$(E1)$	(10^-)	10^+
	422.0	0.80(4)	0.99(5)	$E2$	(12^-)	(10^-)
	494.7	0.69(4)	1.19(6)	$E2$	(14^-)	(12^-)
	569.3	0.53(5)			(16^-)	(14^-)
	610.1	0.50(4)			(18^-)	(16^-)
	645.2	0.43(3)			(20^-)	(18^-)
	695.8	0.36(3)			(22^-)	(20^-)
	752.0	0.27(2)			(24^-)	(22^-)
	802.1	0.18(2)			(26^-)	(24^-)
	832.3	0.14(1)			(28^-)	(26^-)
	794.6	0.06(1)			(30^-)	(28^-)
	847.3	0.05(1)			(32^-)	(30^-)
	928.1	0.04(1)			(34^-)	(32^-)
	1025.0	0.04(1)			(36^-)	(34^-)
Band 7						
7 →yrast	(901)	0.25(15)			(13^+)	12^+
	454.6	0.13(1)			(15^+)	(13^+)
$7 \rightarrow 8$	233.8	0.22(1)			(15^+)	(14^+)
7 →yrast	(764)	0.14(4)			(15^+)	14^+

TABLE I: (continued)

Band	E_γ (keV)	I_γ	R	Multipolarity	$I^\pi_{\rm initial}$	$I^\pi_{\rm final}$
	528.2	0.28(2)			(17^+)	(15^+)
$7 \rightarrow 8$	272.8	0.29(2)			(17^+)	(16^+)
	595.7	0.53(3)			(19^+)	(17^+)
$7 \rightarrow 8$	304.5	0.33(2)			(19^+)	(18^+)
	653.3	0.29(1)			(21^+)	(19^+)
$7 \rightarrow 8$	335.0	0.23(1)			(21^+)	(20^+)
	684.1	0.24(2)			(23^+)	(21^+)
$7 \rightarrow 8$	349.9	0.27(2)			(23^+)	(22^+)
	737.6	0.38(3)			(25^+)	(23^+)
$7 \rightarrow 8$	373.4	0.25(2)			(25^+)	(24^+)
	797.9	0.25(2)			(27^+)	(25^+)
$7 \rightarrow 8$	407.0	0.18(1)			(27^+)	(26^+)
	864.7	0.29(2)			(29^+)	(27^+)
$7 \rightarrow 8$	441.4	0.18(1)			(29^+)	(28^+)
	941.5	0.15(1)			(31^+)	(29^+)
	1014.1	0.14(1)			(33^+)	(31^+)
	1085.1	0.07(1)			(35^+)	(33^+)
Band 8						
$8 \rightarrow 7$	220.8	0.19(2)			(14^+)	(13^+)
	488.3	0.19(1)			(16^+)	(14^+)
$8 \rightarrow 7$	254.1	0.41(3)			(16^+)	(15^+)
	563.8	0.30(2)			(18^+)	(16^+)
$8 \rightarrow 7$	290.6	0.46(2)			(18^+)	(17^+)
	622.8	0.46(2)			(20^+)	(18^+)
$8 \rightarrow 7$	317.9	0.48(2)			(20^+)	(19^+)
	670.4	0.48(2)			(22^+)	(20^+)
$8 \rightarrow 7$	335.0	0.17(4)			(22^+)	(21^+)
	713.2	0.32(3)			(24^+)	(22^+)
$8 \rightarrow 7$	363.3	0.28(2)			(24^+)	(23^+)
	765.1	0.33(2)			(26^+)	(24^+)
$8 \rightarrow 7$	390.6	0.20(1)			(26^+)	(25^+)
	831.3	0.36(3)			(28^+)	(26^+)
$8 \rightarrow 7$	423.3	0.17(5)			(28^+)	(27^+)
	903.4	0.27(2)			(30^+)	(28^+)
	977.7	0.24(2)			(32^+)	(30^+)
	1050.4	0.17(2)			(34^+)	(32^+)
	1115.6	0.14(1)			(36^+)	(34^+)
	1170.4	0.10(1)			(38^+)	(36^+)
Band 9						
$9 \rightarrow$yrast	991.2	0.43(19)			(5^-)	6^+
	394.1	0.42(3)			7^-	(5^-)
$9 \rightarrow$yrast	1386.4	1.05(4)	0.53(41)	$E1$	7^-	6^+
$9 \rightarrow$yrast	922.5	0.52(4)			7^-	8^+
	378.6	0.57(9)			9^-	7^-
$9 \rightarrow 10$	203.8	1.32(4)	0.26(18)	$M1/E2$	9^-	8^-
	463.3	0.68(7)			11^-	9^-
$9 \rightarrow 10$	234.7	0.38(3)	0.77(46)	$M1/E2$	11^-	10^-
	532.3	0.42(8)			(13^-)	11^-
$9 \rightarrow 10$	250.9	0.17(4)			(13^-)	(12^-)
	564.8	0.39(9)			(15^-)	(13^-)
$9 \rightarrow 10$	239.4	0.04(1)			(15^-)	(14^-)
	595.6	0.92(3)			(17^-)	(15^-)
$9 \rightarrow 10$	234.8	0.46(2)			(17^-)	(16^-)
	562.9	0.48(8)			(19^-)	(17^-)
$9 \rightarrow 10$	292.3	0.53(4)			(19^-)	(18^-)
	650.6	0.72(2)			(21^-)	(19^-)
$9 \rightarrow 10$	336.4	0.18(3)			(21^-)	(20^-)
	733.7	0.79(3)			(23^-)	(21^-)
$9 \rightarrow 10$	375.6	0.11(1)			(23^-)	(22^-)

TABLE I: (continued)

Band	E_γ (keV)	I_γ	R	Multipolarity	$I^\pi_{\rm initial}$	$I^\pi_{\rm final}$
	805.7	0.28(3)			(25^-)	(23^-)
	869.5	0.23(1)			(27^-)	(25^-)
	926.8	0.21(1)			(29^-)	(27^-)
	979.2	0.18(1)			(31^-)	(29^-)
	1035.1	0.10(1)			(33^-)	(31^-)
	1076.6	0.10(1)			(35^-)	(33^-)
Band 10						
$10 \rightarrow 9$	174.9	1.81(17)	0.61(38)	$M1/E2$	8^-	7^-
	430.6	0.80(6)			10^-	8^-
$10 \rightarrow 9$	226.4	1.10(6)	0.28(26)	$M1/E2$	10^-	9^-
	519.8	0.50(12)			(12^-)	10^-
$10 \rightarrow 9$	281.4	0.39(6)			(12^-)	11^-
	573.7	0.06(1)			(14^-)	(12^-)
$10 \rightarrow 9$	325.7	0.05(1)			(14^-)	(13^-)
	599.5	0.24(6)			(16^-)	(14^-)
$10 \rightarrow 9$	359.7	0.05(2)			(16^-)	(15^-)
	504.4	0.11(2)			(18^-)	(16^-)
$10 \rightarrow 9$	269.7	0.05(1)			(18^-)	(17^-)
	607.9	0.42(9)			(20^-)	(18^-)
$10 \rightarrow 9$	315.6	0.52(4)			(20^-)	(19^-)
	694.9	0.28(5)			(22^-)	(20^-)
$10 \rightarrow 9$	358.4	0.12(2)			(22^-)	(21^-)
	770.7	0.25(2)			(24^-)	(22^-)
	840.0	0.21(3)			(26^-)	(24^-)
	898.6	0.18(1)			(28^-)	(26^-)
	954.3	0.11(1)			(30^-)	(28^-)
	1003.4	0.10(1)			(32^-)	(30^-)
	1054.9	0.08(1)			(34^-)	(32^-)
Band 11						
$11 \rightarrow 9$	323.8	0.25(8)			(10^-)	(9^-)
	335.2	0.11(2)			(12^-)	(10^-)
$11 \rightarrow 9$	194.5	0.36(4)			(12^-)	11^-
$11 \rightarrow 12$	162.9	0.49(2)			(12^-)	(11^-)
$11 \rightarrow 10$	430.0	0.30(2)			(12^-)	10^-
	444.4	1.49(4)			(14^-)	(12^-)
$11 \rightarrow 12$	236.8	0.24(1)			(14^-)	(13^-)
	536.2	1.64(5)			(16^-)	(14^-)
$11 \rightarrow 12$	(284)	0.09(4)			(16^-)	(15^-)
	613.9	1.58(13)			(18^-)	(16^-)
	676.2	1.10(10)			(20^-)	(18^-)
	724.1	0.42(11)			(22^-)	(20^-)
	760.5	0.19(8)			(24^-)	(22^-)
	(804)	0.14(8)			(26^-)	(24^-)
	(839)	0.11(8)			(28^-)	(26^-)
Band 12						
$12 \rightarrow 10$	266.7	0.43(4)			(11^-)	10^-
$12 \rightarrow 9$	494.4	0.55(9)			(11^-)	9^-
	372.1	0.26(2)			(13^-)	(11^-)
$12 \rightarrow 11$	209.7	0.65(3)			(13^-)	(12^-)
$12 \rightarrow 9$	403.4	0.48(3)			(13^-)	11^-
	(489)	0.05(1)			(15^-)	(13^-)
$12 \rightarrow 11$	(252)	0.02(1)			(15^-)	(14^-)
	(578)	0.13(1)			(17^-)	(15^-)
$12 \rightarrow 11$	(294)	0.24(5)			(17^-)	(16^-)
	(648)	0.52(12)			(19^-)	(17^-)

[a] Ref. [21].

TABLE II: The energies of the candidate TSD bands in ^{160}Er in keV. The γ-ray energies are estimated to be accurate to $\sim \pm 0.6$ keV.

TSD 1	TSD 2	TSD 3
1017.3	(947)	828.7
1061.7	1001.9	848.4
1100.0	1054.4	890.2
1140.4	1098.3	939.5
1185.6	1138.0	991.1
1233.4	1185.6	1048.7
1286.2	1242.8	1110.7
1346.2	1305.1	1166.3
1406.9	1387.2	1232.8
1474.1	1470.1	(1303)
1532.3	(1568)	(1375)
(1593)		(1456)
(1666)		

TABLE III: Quasiparticle labeling scheme for ^{160}Er based on the predominant Nilsson components at $\hbar\omega = 0$ MeV and their parity and signature (π, α). Note that the $\nu h_{9/2}$ and $f_{7/2}$ orbitals are highly mixed.

	Label	$(\pi, \alpha)_n$	Nilsson orbital at $\hbar\omega = 0$ MeV
Quasineutrons	A	$(+, +1/2)_1$	$i_{13/2}[651]3/2$
	B	$(+, -1/2)_1$	$i_{13/2}[651]3/2$
	C	$(+, +1/2)_2$	$i_{13/2}[660]1/2$
	D	$(+, -1/2)_2$	$i_{13/2}[660]1/2$
	E	$(-, +1/2)_1$	$h_{9/2}[521]3/2$
	F	$(-, -1/2)_1$	$h_{9/2}[521]3/2$
	G	$(-, -1/2)_2$	$f_{7/2}[523]5/2$
	H	$(-, +1/2)_2$	$f_{7/2}[523]5/2$
Quasiprotons	A_p	$(-, -1/2)_1$	$h_{11/2}[523]7/2$
	B_p	$(-, +1/2)_1$	$h_{11/2}[523]7/2$
	E_p	$(+, -1/2)_1$	$g_{7/2}[404]7/2$
	F_p	$(+, +1/2)_1$	$g_{7/2}[404]7/2$

TABLE IV: A summary of the quasi-particle configurations proposed for the bands observed in ^{160}Er.

Band	Configurations
Yrast	$0 \rightarrow AB \rightarrow AB \otimes A_pB_p$ and EF and/or CD
1	$AF \rightarrow AFBC \rightarrow AFBC \otimes A_pB_p$
2	$AE \rightarrow AEBC \rightarrow AEBC \otimes A_pB_p$
3	$0 \rightarrow BCAD \rightarrow BCAD \otimes A_pB_p$ and/or EF
4	$\beta \rightarrow \beta \otimes AB$
5	$\gamma \rightarrow \gamma \otimes AB \rightarrow \gamma \otimes AB \otimes A_pB_p$
6	$AG \rightarrow AGBC \rightarrow AGBC \otimes A_pB_p$
7 and 8	$AE \otimes A_pE_p(F_p) \rightarrow AEBC \otimes A_pE_p(F_p)$
9 and 10	$A_pE_p(F_p) \rightarrow AB \otimes A_pE_p(F_p)$
11 and 12	$AF \otimes A_pE_p(F_p)$